

# Superconductivity in the spin-state crossover materials: Nickelates with planar-coordinated low-spin $\text{Ni}^{2+}$ ions

Jiří Chaloupka<sup>1</sup> and Giniyat Khaliullin<sup>2</sup>

<sup>1</sup>*Department of Condensed Matter Physics, Faculty of Science,  
Masaryk University, Kotlářská 2, 61137 Brno, Czech Republic*

<sup>2</sup>*Max Planck Institute for Solid State Research, Heisenbergstrasse 1, D-70569 Stuttgart, Germany*  
(Dated: June 23, 2025)

We theoretically study quasi-two-dimensional nickel compounds, where the nickel ions assume  $\text{Ni}^{2+}$   $d^8$  valence state and feature a low-spin  $S = 0$  ground state quasidegenerate with  $S = 1$  ionic excitations. Such a level structure is supported by square-planar coordination of nickel ions or a suitable substitution of apical oxygens. We construct the corresponding singlet-triplet exchange model and explore its phase diagram and excitation spectrum. By hole doping, we further introduce mobile  $\text{Ni}^{3+}$   $d^7$  ionic configurations with effective spins  $S = 1/2$ , and analyze their interactions with the  $d^8$  singlet-triplet background. The interplay with the triplet excitations in the  $d^8$  sector is found to have a deep impact on the propagation of the doped hole-like charge carriers and is identified as a powerful source of Cooper pairing among them.

## I. INTRODUCTION

After decades of efforts to find cuprate-like superconductivity (SC) in nickel-based compounds, unconventional SC has finally been discovered in a number of nickelate families in recent years [1–8]. It is truly remarkable that the Ni valence states, orbital degeneracy, and fermiology vary broadly among the nickelate superconductors: While  $\text{NdNiO}_2$  discovered in 2019 [1] apparently falls well into the cuprate’s “single-layer, single-orbital, spin one-half” paradigm, the bilayer  $\text{La}_3\text{Ni}_2\text{O}_7$  [2] and trilayer  $\text{La}_4\text{Ni}_3\text{O}_{10}$  [6, 7] nickelate SCs seem greatly differ from cuprates in all respects. Indeed, (i) in contrast to only weakly coupled  $\text{CuO}_2$  planes in cuprates, the  $\text{NiO}_2$  planes are tightly bound into bilayers or trilayers in them; (ii) distinct from cuprates, both  $e_g$  orbitals  $x^2 - y^2$  and  $3z^2 - r^2$  are essential; and, finally, (iii) Ni-valence is far from the cuprate-like spin one-half  $d^9$  configuration, but rather in the mixed-valence regime with  $\sim 7.5$  electrons in the  $3d$  shell. Such a diversity of Ni-based SCs should be related to the rich spin-and-orbital physics typical for nickelates, and suggests that more superconductors may be found in the future among the nickel-based materials with different lattice and orbital structures.

One well-known consequence of the orbital degeneracy in compounds of transition metal ions such as Fe, Co, and Ni are the famous spin-state crossover phenomena [9]. In spin-crossover materials, a close competition between the lattice crystalline fields and intraionic Hund’s coupling results in the quasi-degeneracy of the ionic spin states. For example, the  $\text{Ni}^{2+}$  ion with  $d^8$  configuration may adopt either  $S = 0$  singlet or  $S = 1$  triplet ground state, as illustrated in Fig. 1(a). Importantly, the ground state spin value depends sensitively on the lattice structure details, covalency, etc, and can thus be tuned by external factors such as pressure or strain [10]. The spin-state quasi-degeneracy is quite common phenomena among the  $\text{Ni}^{2+}$  compounds with various lattice structures, e.g.,  $\text{Sr}_2\text{NiO}_2\text{Cu}_2(\text{S,Se})_2$  [11–13],

$(\text{Sr,Ba})_2\text{NiO}_2\text{Ag}_2\text{Se}_2$  [14],  $\text{BaNiO}_2$  [15],  $\text{LaNiO}_{2.5}$  [16].

In this paper we perform a model exploration of single-layer nickelates in the spin-state crossover regime. Specifically, we consider low-spin  $\text{Ni}^{2+}$   $d^8$  Mott insulators doped by mobile hole-like charge carriers, and address the question of pairing mechanisms and possible superconductivity in them. We find that the doped holes strongly interact with the spin-state fluctuations, namely, while moving they emit and absorb singlet-triplet excitations. This leads to polaron physics similar to that in the electron-phonon problem, and gives rise to an effective attraction between the charge carriers. We analyze and evaluate various pairing processes, and conclude that the nickel-based spin-crossover materials are promising candidates to host high-temperature superconductivity.

The paper is organized as follows: Section II derives the exchange model for the undoped Mott insulator with low-spin  $\text{Ni}^{2+}$   $d^8$  ions (Sec. II A), and presents its phase diagram along with a cross-check against exact diagonalization of the underlying Hubbard model (Sec. II B). The mobile  $d^7$  hole-like carriers are considered in Sec. III: we first introduce the interactions between the holes and the  $d^8$  background (Sec. III A), then analyze the single-particle propagation of the doped holes at low densities (Sec. III B), and finally move on to the central topic of the paper—a study of the mechanisms of Cooper pairing among the holes (Sec. III C). Section IV concludes the paper.

## II. LOW-SPIN $\text{Ni}^{2+}$ $d^8$ INSULATOR

We construct our model as a low-energy effective model of the Hubbard model based on  $e_g$  orbitals. We assume that crystal field splitting  $\Delta$  between  $x^2 - y^2$  and  $3z^2 - r^2$  orbitals [Fig. 1(b)] is sufficient to compensate the Hund’s coupling  $J_H$  and stabilize spin-singlet ground state. It is important to note at this point that  $J_H$  in a solid is well reduced from its free-ion value due to covalency effects.

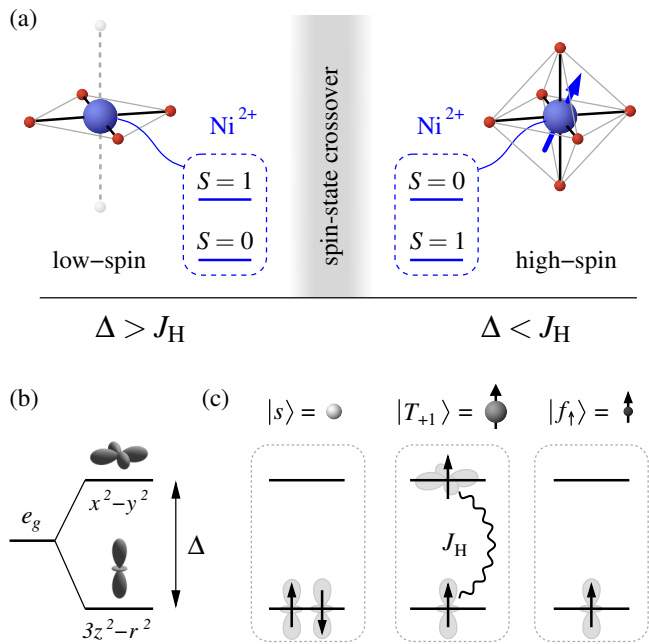


FIG. 1. (a) Ground-state spin configuration of a  $\text{Ni}^{2+}$  ion with  $d^8(t_{2g}^6 e_g^2)$  electronic filling, tuned by the competition of Hund's coupling  $J_H$  and the crystal field splitting  $\Delta$ . If the  $\text{Ni}^{2+}$  ion is planar-coordinated or placed into a highly elongated oxygen octahedra, it would assume a singlet ground state with doubly occupied  $3z^2 - r^2$  orbital. (b) Splitting of  $e_g$  orbital levels in a crystal field promoting the above low-spin configuration. (c) Low-energy states selected as a basis of our effective model:  $d^8$  singlet  $s$  with doubly occupied  $3z^2 - r^2$  orbital,  $d^8$  triplet  $T$ , where the CF splitting  $\Delta$  is nearly compensated by Hund's coupling  $J_H$ , and  $d^7$  state corresponding to the hole-like particle  $f$  with spin one-half.

We further assume that the balance between  $\Delta$  and  $J_H$  is such that while the ground state of  $\text{Ni}^{2+}$  is non-magnetic, the excited spin-triplet states are still nearby in energy. In this regime, the relevant basis states are those depicted in Fig. 1(c). As a first step, we consider the non-doped case with  $d^8$  ( $t_{2g}^6 e_g^2$ ) electronic configuration, and study the corresponding exchange model based on the ionic singlet  $s$  and triplet  $T$  states.

### A. Exchange model

Built on top of a  $t_{2g}^6$  configuration, which is considered rigid, the basis states  $s$  and  $T$  are obtained by diagonalizing the on-site Coulomb interaction between the two additional  $e_g$  electrons, as embedded in the local part of the  $e_g$  Hubbard model:

$$\frac{1}{2}\Delta(n_x - n_z) + U(n_{x\uparrow}n_{x\downarrow} + n_{z\uparrow}n_{z\downarrow}) + (U - \frac{5}{2}J_H)n_x n_z - 2J_H \mathbf{S}_x \mathbf{S}_z + J_H(x_{\uparrow}^{\dagger}x_{\downarrow}^{\dagger}z_{\downarrow}z_{\uparrow} + z_{\uparrow}^{\dagger}z_{\downarrow}^{\dagger}x_{\downarrow}x_{\uparrow}). \quad (1)$$

Here we have introduced a shorthand notation by denoting the electron operators  $d_{x^2-y^2}$  and  $d_{3z^2-r^2}$  as  $x$  and

$z$ , respectively. Due to the pair hopping term  $\propto J_H$ , the singlet ground state  $|s\rangle$  is actually a linear combination

$$|s\rangle = (\cos\theta z_{\uparrow}^{\dagger}z_{\downarrow}^{\dagger} - \sin\theta x_{\uparrow}^{\dagger}x_{\downarrow}^{\dagger}) |t_{2g}^6\rangle \quad (2)$$

with  $\theta$  given by  $\tan 2\theta = J_H/\Delta$ . In the regime of our interest,  $\theta$  is small and most of the weight is carried by the pair of electrons in  $3z^2 - r^2$  orbital as indicated in Fig. 1(c). The three members of the triplet  $T$  read simply as

$$\begin{aligned} |T_{+1}\rangle &= x_{\uparrow}^{\dagger}z_{\uparrow}^{\dagger} |t_{2g}^6\rangle, \\ |T_0\rangle &= \frac{1}{\sqrt{2}}(x_{\uparrow}^{\dagger}z_{\downarrow}^{\dagger} + x_{\downarrow}^{\dagger}z_{\uparrow}^{\dagger}) |t_{2g}^6\rangle, \\ |T_{-1}\rangle &= x_{\downarrow}^{\dagger}z_{\downarrow}^{\dagger} |t_{2g}^6\rangle. \end{aligned} \quad (3)$$

The energy splitting between the above states is an essential parameter of our model. Based solely on the ionic Hamiltonian, we get for the singlet-triplet splitting

$$E_T = E(|T\rangle) - E(|s\rangle) = \sqrt{\Delta^2 + J_H^2} - 3J_H. \quad (4)$$

In reality, this splitting is influenced by various factors beyond the ionic Hamiltonian, for example covalency effects, and may be therefore regarded as a free parameter. However, for simplicity we will maintain the connection to the  $e_g$  Hubbard model and use Eq. (4) hereafter. Note, that if the pair hopping term is omitted, we get the familiar expression  $\Delta - 3J_H$  for  $E_T$ .

The exchange interactions among  $d^8$  ions are derived in the usual way by perturbatively eliminating the intersite hopping to second order. In the case of  $e_g$  orbitals on the square lattice, the hopping at nearest-neighbor bond  $ij$  takes the following form fixed by Slater-Koster rules:

$$-t \left[ x^{\dagger}x + \frac{1}{3}z^{\dagger}z \mp \frac{1}{\sqrt{3}}(x^{\dagger}z + z^{\dagger}x) \right]_{ij}. \quad (5)$$

We parametrize the hopping by the larger amplitude  $t$  for the planar  $x^2 - y^2$  orbitals. The doped holes to be introduced later will reside in  $3z^2 - r^2$  orbitals, having thus a significantly reduced bandwidth determined by  $t/3$ . The sign ( $\mp$ ) of the interorbital hopping is linked to the bond direction:  $-$  is applied at  $x$  bonds,  $+$  at  $y$  bonds.

The exchange interactions are most intuitively depicted as bond processes involving  $s$  (scalar) and  $\mathbf{T}$  (vector) hardcore bosons representing the singlet and triplet  $d^8$  states. The hardcore bosons  $\mathbf{T}$  are hereafter referred to as *triplons*. Such a hardcore-boson representation is used in Fig. 2(a),(b), where we show a few examples of the rather rich possibilities to be discussed later. Fortunately, due to the inherent spin-isotropy imposed by the underlying Hubbard model, the exchange interactions have to obey spin conservation rules, which limits the number of independent model parameters. To express the resulting  $d^8$  model Hamiltonian in a compact form, we utilize several auxiliary vector operators based on the

following Cartesian combinations of the triplet states:

$$\begin{aligned} |T_x\rangle &= \frac{i}{\sqrt{2}}(|T_{+1}\rangle - |T_{-1}\rangle), \\ |T_y\rangle &= \frac{1}{\sqrt{2}}(|T_{+1}\rangle + |T_{-1}\rangle), \\ |T_z\rangle &= -i|T_0\rangle. \end{aligned} \quad (6)$$

The first vector operator  $\tilde{\mathbf{S}} = (\tilde{S}^x, \tilde{S}^y, \tilde{S}^z)$  is local and is associated with the on-site  $s \leftrightarrow T$  transition:

$$\tilde{S}^\alpha = -i(s^\dagger T_\alpha - T_\alpha^\dagger s), \quad \alpha = x, y, z. \quad (7)$$

The second local operator  $\mathbf{S} = (S^x, S^y, S^z)$  directly corresponds to the spin-1 carried by  $\mathbf{T}$  and is defined by

$$S^\alpha = -i\epsilon_{\alpha\beta\gamma} T_\beta^\dagger T_\gamma, \quad \text{i.e. } \mathbf{S} = -i(\mathbf{T}^\dagger \times \mathbf{T}). \quad (8)$$

We also introduce analogous bond operators having the internal structure identical to  $\tilde{\mathbf{S}}$  and  $\mathbf{S}$ :

$$\tilde{S}_{ji}^\alpha = -i(s_j^\dagger T_{\alpha i} - T_{\alpha j}^\dagger s_i), \quad S_{ji}^\alpha = -i\epsilon_{\alpha\beta\gamma} T_{\beta j}^\dagger T_{\gamma i}. \quad (9)$$

The above operators enable us to express the  $d^8$  model Hamiltonian in a manifestly spin-isotropic compact form

$$\begin{aligned} \mathcal{H}_{d^8} &= E_T \sum_i n_{T_i} + \kappa \sum_{\langle ij \rangle} \tilde{\mathbf{S}}_i \tilde{\mathbf{S}}_j \\ &+ \sum_{\langle ij \rangle} \left[ \text{sgn}_{ij} K(\tilde{\mathbf{S}}_{ij} \mathbf{S}_{ji} + \mathbf{S}_{ij} \tilde{\mathbf{S}}_{ji}) + J \mathbf{S}_i \mathbf{S}_j \right]. \end{aligned} \quad (10)$$

Here the first term counts the number of triplons via  $n_T = \sum_{\alpha=x,y,z} T_\alpha^\dagger T_\alpha$  and penalizes them by the energy  $E_T$ , the other terms represent the exchange interactions being sorted as second, third, and fourth-order contributions in  $T$  operators, i.e. according to their expected relevance at low triplon density. Due to  $e_g$  orbital symmetry, there is sensitivity to the bond direction inherited from the hopping (5). It is captured by the bond-dependent sign factor  $\text{sgn}_{ij}$ , which is equal to  $+1$  or  $-1$  for  $x$  and  $y$  bonds, respectively. Finally, when rewriting the operators in the  $K$  term using the elementary hardcore-boson operators  $s$  and  $\mathbf{T}$ , these have to be taken in normal order with the creation operators moved to the left.

We now briefly discuss the rather complex exchange processes contained in (10) with the help of the cartoon representations in Fig. 2(a),(b), capturing the exchange in the form of a generation, propagation, and mutual interactions of hardcore triplet particles  $\mathbf{T}$  in a background made of  $s$ . The  $\kappa$ -term  $\tilde{\mathbf{S}}_i \tilde{\mathbf{S}}_j$  includes two distinct types of processes depicted in Fig. 2(a). The first is a creation and annihilation of singlet pairs of  $\mathbf{T}$  on bonds, corresponding to a combination  $T_x T_x + T_y T_y + T_z T_z = T_{+1} T_{-1} - T_0 T_0 + T_{-1} T_{+1}$ . The other one is a simple  $\mathbf{T}$  hopping preserving the  $T$  label (either  $\pm 1, 0$  or Cartesian  $x, y, z$ ). The relative amplitude of these processes is fixed to  $-1$  by the interaction term. Being of second order in  $T$  operators, this is the most important exchange interaction at low triplon concentration of about  $n_T \lesssim 0.2$  per

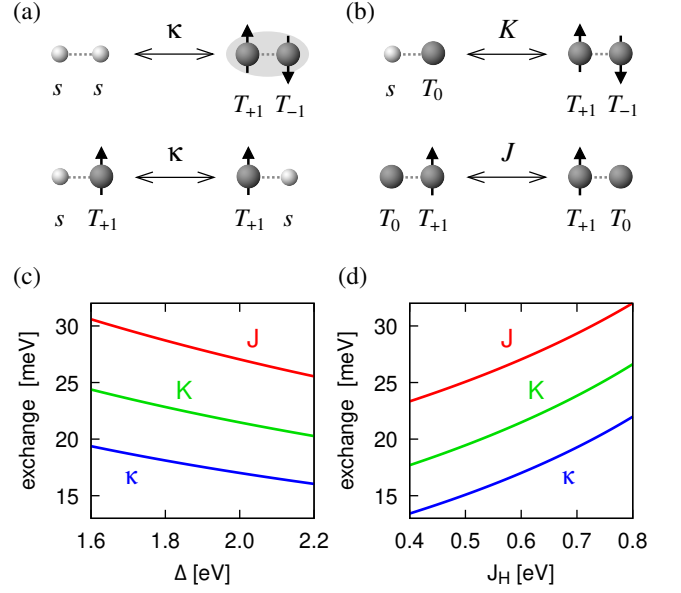


FIG. 2. (a) Examples of exchange processes among the  $d^8$  ions contributing to the  $\kappa$  interaction channel of  $\mathcal{H}_{d^8}$  of Eq. (10). There are two distinct classes of processes—creation/annihilation of singlet pairs of triplons  $\mathbf{T}$  (top) and  $\mathbf{T}$  hopping in the  $s$  background (bottom). (b) Sample processes contained in the higher-order channels  $K$  and  $J$  of  $\mathcal{H}_{d^8}$ . (c) Exchange parameters entering Eq. (10) as obtained by second-order perturbation theory [see Eq. (11)] assuming  $U = 5$  eV,  $J_H = 0.6$  eV, and  $t = 0.3$  eV. (d) The same for fixed  $\Delta = 2$  eV and varying  $J_H$ .

site. The third-order  $K$  contribution may be understood as an  $s \leftrightarrow T$  transition entangled with the spin-1 of another  $\mathbf{T}$  particle, while the fourth-order  $J$  term is just the regular Heisenberg exchange between the spins-1 carried by  $\mathbf{T}$ . Two examples of such higher-order processes are presented in Fig. 2(b).

Through the perturbative calculation, one arrives at two more contributions not explicitly included in (10): (i) a small renormalization of  $E_T$  level, (ii) repulsion between  $T$  particles. Both are marginal, opposing each other, and can be safely absorbed into  $E_T$  (the latter one on a mean-field level), so that they do not alter the form of the  $d^8$  model (10).

The overall phase behavior of the  $d^8$  model (10) is driven by the competition between the triplon cost  $E_T$  and the strength of the exchange interactions that profit from the presence of the triplons and eventually lead to their condensation. The microscopic derivation provides the following values of the three exchange parameters:

$$\begin{aligned} \kappa &= \frac{t^2}{3} \left( \frac{1 + \cos 2\theta}{E_{-1}} + \frac{2 \sin 2\theta}{E_0} + \frac{1 - \cos 2\theta}{E_{+1}} \right), \\ K &= \frac{2\sqrt{2}t^2}{3\sqrt{3}} \left[ \left( \frac{1}{E_{-1}} + \frac{1}{E_0} \right) \cos \theta + \left( \frac{1}{E_{+1}} + \frac{1}{E_0} \right) \sin \theta \right], \\ J &= \frac{t^2}{3} \left( \frac{1}{E_{-1}} + \frac{10}{3E_0} + \frac{1}{E_{+1}} \right), \end{aligned} \quad (11)$$

where the denominators contain virtual energies  $E_n = U + n\Delta + J_H + 2E_T$  ( $n = 0, \pm 1$ ) in the intermediate states. Plotted in Fig. 2(c),(d) are the exchange constants evaluated for representative values of the microscopic parameters. For the Ni ions, we assume  $U = 5$  eV and  $J_H = 0.6$  eV throughout the paper, the crystal-field splitting  $\Delta$  is varied around 2 eV, leading to quasidegenerate  $s$  and  $T$  levels. The hopping  $t$  is set to a representative value of 0.3 eV in Fig. 2. The values of  $\kappa$ ,  $K$ , and  $J$  observed in Fig. 2(c),(d) are relatively robust to variations in  $\Delta$  and  $J_H$ . This is caused by the dominating values of  $U + n\Delta$  in the denominators in (11), which are only little affected by changes  $\Delta$  and  $J_H$  within the ranges shown. In the presented parameter regime we get the hierarchy  $J > K > \kappa$ , which, however, needs to be considered together with the different role of these interactions. Even though  $J$  and  $K$  are larger than  $\kappa$ , they are of higher order in  $T$  operators and thus relevant only at larger concentration  $n_T$  of triplons. In addition, to activate  $J$  and  $K$  interactions, a prior presence of triplons is necessary, while  $\kappa$  interaction channel generates them itself. In some of the cases discussed later, it will be thus sufficient to study a simplified model including  $E_T$  and  $\kappa$  terms only.

## B. Phase diagram and excitations

A basic exploration of the phase behavior of the singlet-triplet model and its excitation spectrum can be performed using the methods developed in the context of spin ladders or bilayer magnets, where the singlet-triplet basis is hosted by Heisenberg rungs connecting the rails or layers [17–20]. The possibility of triplon condensation at a sufficient exchange strength is addressed using the variational Ansatz

$$|\Psi\rangle = \prod_{\mathbf{R}} \left[ \sqrt{1-\rho} s^\dagger + \sqrt{\rho} (\mathbf{u} - i\mathbf{v}) \mathbf{T}^\dagger \right]_{\mathbf{R}} |\text{vac}\rangle. \quad (12)$$

The energy obtained by averaging the Hamiltonian (10) in the trial state (12)

$$\begin{aligned} E_{\text{avg}} = E_T \sum_i \rho + \sum_{\langle ij \rangle} \left\{ 4\kappa\rho(1-\rho) \mathbf{v}_i \mathbf{v}_j \right. \\ \left. - \text{sgn}_{ij} K\rho\sqrt{\rho(1-\rho)} [\mathbf{v}_i(\mathbf{u} \times \mathbf{v})_j + (\mathbf{u} \times \mathbf{v})_i \mathbf{v}_j] \right. \\ \left. + 4J\rho^2 (\mathbf{u} \times \mathbf{v})_i (\mathbf{u} \times \mathbf{v})_j \right\} \quad (13) \end{aligned}$$

is to be minimized with respect to the condensate density  $0 \leq \rho \leq 1$  and site-dependent real vectors  $\mathbf{u}$ ,  $\mathbf{v}$  that obey the condition  $\mathbf{u}^2 + \mathbf{v}^2 = 1$ . This approach does not include quantum fluctuations but still gives a semi-quantitatively correct picture, as we will demonstrate later by cross checking with the exact diagonalization of the underlying Hubbard model.

Presented in Fig. 3(a) is the variational phase diagram obtained by varying the microscopic parameters  $\Delta$  and

$t$  and evaluating the effective model parameters  $E_T$ ,  $\kappa$ ,  $K$ ,  $J$  via Eqs. (4) and (11). The variational approach identifies three phases described in the following.

In the paramagnetic (PM) phase, the condensate is absent ( $\rho = 0$ ) and triplons  $\mathbf{T}$  correspond to gapped elementary excitations. Their dispersion can be obtained by starting with  $\mathcal{H}_{d^8}$  of Eq. (10), making the replacement  $s, s^\dagger \rightarrow \sqrt{1-n_T}$  to account for the hardcore constraint, and expanding the result in  $T_\alpha, T_\alpha^\dagger$  operators. Afterwards,  $\mathbf{T}$  are treated as unconstrained bosons. At the same level of approximation as used when constructing the phase diagram itself, the expansion is performed to second order and the approximate Hamiltonian is readily solved by Fourier and Bogoliubov transformations. This standard procedure [19] gives a three-fold degenerate dispersion

$$\omega_{\mathbf{q}} = \sqrt{E_T(E_T + 8\kappa\gamma_{\mathbf{q}})} \quad (14)$$

with  $\gamma_{\mathbf{q}} = \frac{1}{2}(\cos q_x + \cos q_y)$ , visualized in Fig. 3(b) for a few sample points in the PM phase. As the exchange strength increases, following the increase of  $t$ , the excitations gradually soften at the momentum  $(\pi, \pi)$ . When the critical point  $E_T = 8\kappa$  is reached, the excitation gap closes, signaling a condensation of triplons and the emergence of long-range order. The observation of the above excitations, e.g. by neutron scattering, would be an important experimental test of our model and would provide a valuable input for its quantification in a particular material. We also note that a significant broadening of the triplons due to their mutual interactions as well as interactions with doped carriers can be expected.

In the new phase, labeled by FQ in Fig. 3(a), the optimization of the variational Ansatz (12) leads to a nonzero condensate density  $\rho$ . The condensate structure is given by staggered  $\mathbf{v}_{\mathbf{R}} = \mathbf{v} e^{i\mathbf{Q}\mathbf{R}}$  with  $\mathbf{Q} = (\pi, \pi)$  and zero  $\mathbf{u}$ . The corresponding energy per site derived from (13) takes the value  $E_{\text{FQ}} = -2\kappa(1 - E_T/8\kappa)^2$  and does not include  $K$  and  $J$  as these contribute at higher order via quantum fluctuations. Based on the above condensate structure, the phase is characterized by long-range correlations of the auxiliary quantity  $\tilde{\mathbf{S}} \propto \mathbf{v}$  with the characteristic momentum  $\mathbf{Q}$  and nonzero average  $\langle \tilde{\mathbf{S}} \rangle_{\mathbf{q}=\mathbf{Q}}$  acting as an order parameter. In terms of the measurable spin-1 carried by  $\mathbf{T}$ , one gets the average  $\langle S^\alpha S^\beta \rangle_{\mathbf{q}=0} = \rho(\delta_{\alpha\beta} - v_\alpha v_\beta)$  corresponding to a ferroquadrupolar (FQ) order, where  $\mathbf{v}$  plays the role of the director. Note, however, that the primary order parameter is the above  $\langle \tilde{\mathbf{S}} \rangle_{\mathbf{q}=\mathbf{Q}}$  and the FQ spin-1 correlations are reduced by having  $\mathbf{T}$  mixed with still prevailing  $s$ .

Finally, if the triplon cost  $E_T$  is low enough, the system switches into a fully saturated antiferromagnetic (AF) phase with  $\rho = 1$ , i.e. each site is occupied by spin-1  $\mathbf{T}$  particle. This transition may be thus interpreted as the spin-state crossover between the low-spin and high-spin state of  $d^8$ , realized in our approximation by a level crossing. Using Eq. (13), the AF phase gives the average energy per site  $E_{\text{AF}} = E_T - 2J$ , which has to be com-

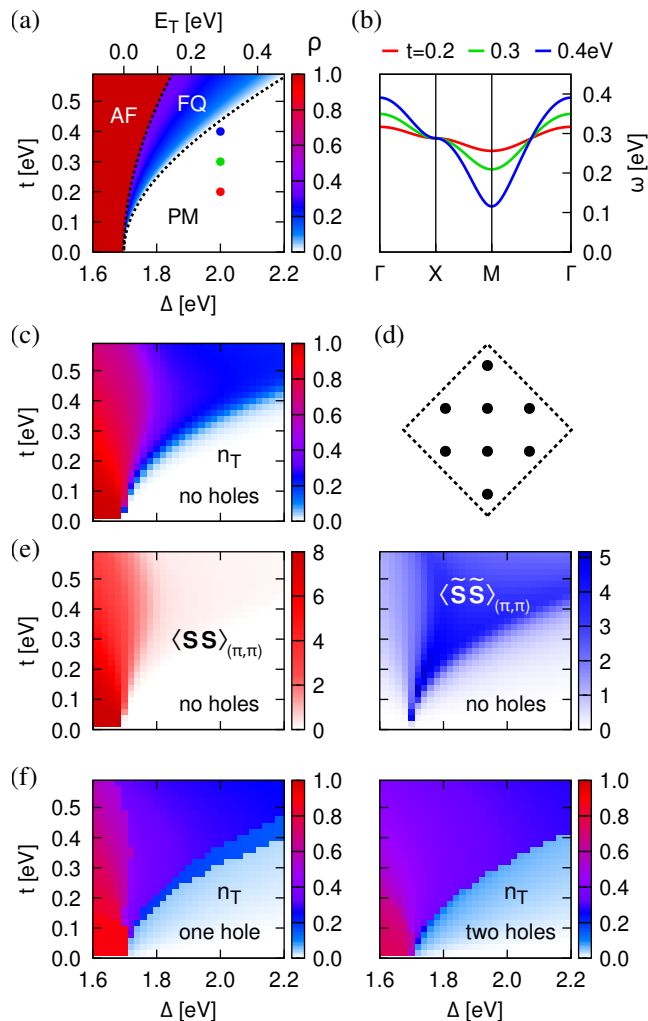


FIG. 3. (a) Phase diagram of the  $d^8$  model in Eq. (10) obtained by a variational estimate based on the trial state (12). Shown is the condensate density  $\rho$  which equals zero in the PM phase, saturates around 0.3 in the FQ phase and jumps to  $\approx 1$  upon entering the AF phase. The model parameters are given by Eqs. (4) and (11) evaluated for  $U = 5$  eV,  $J_H = 0.6$  eV and variable  $\Delta$  and  $t$ . (b) Triplon  $\mathbf{T}$  dispersion in PM phase calculated for the three parameter points marked in (a) ( $\Delta = 2$  eV and  $t = 0.2, 0.3$  or  $0.4$  eV) and plotted along the path connecting the high-symmetry points  $\Gamma = (0, 0)$ ,  $X = (\pi, 0)$ , and  $M = (\pi, \pi)$  in the Brillouin zone. At the PM/FQ boundary, the dispersion becomes gapless at the  $M$  point. (c) Triplon number per site  $n_T$  obtained by exact diagonalization of the  $e_g$  Hubbard model for the 8-site cluster shown in (d). (e) Characteristic correlations in the cluster ground state revealing the tendencies towards long-range ordering—either AF (left) or FQ (right). (f) The same as in (c) but calculated for a reduced number of electrons on the cluster to effectively create 1 or 2 holes.

pared with  $E_{FQ}$  to find the transition line observed in Fig. 3(a). Following the AF/FQ phase boundary from the large  $t$  to small  $t$  limit, we find the associated step in the  $\mathbf{T}$  density increasingly pronounced, reaching maximum at  $t = 0$ , where we hit the point corresponding

to  $E_T = 0$ . This point is a trivially exact point of the phase diagram—here  $E_T$  changes sign and in the absence of exchange interactions due to  $t = 0$ , the system immediately switches between the state consisting exclusively of either  $s$  or  $\mathbf{T}$ .

To assess the adequacy of the effective model and its simple variational treatment, we performed exact diagonalization of the two-orbital Hubbard model with  $e_g$ -type hopping on a small square-lattice cluster. The first set of data to compare to the variational phase diagram is presented in Fig. 3(c). It shows the average triplet occupation  $n_T$  per site calculated for the 8-site cluster of Fig. 3(d) by employing the same microscopic parameters  $\Delta$ ,  $t$ ,  $U$ , and  $J_H$  as those used to construct Fig. 3(a). Note that, in contrast to  $\rho$  of Fig. 3(a),  $n_T$  of Fig. 3(c) includes also the fluctuating part of  $\mathbf{T}$  density. While the map of  $n_T$  itself gives already a good idea of the phase diagram, to reliably identify the phases, we check the tendency towards long-range order by calculating the characteristic correlations  $\langle \mathbf{S}\mathbf{S} \rangle_{q=Q}$  and  $\langle \tilde{\mathbf{S}}\tilde{\mathbf{S}} \rangle_{q=Q}$  associated with the AF and FQ phases, respectively. Shown in Fig. 3(e) are the ground-state values of the correlations evaluated according to  $\langle \mathbf{S}\mathbf{S} \rangle_q = N_{\text{site}}^{-1} \sum_{j \neq j'} e^{iq(\mathbf{R}_j - \mathbf{R}_{j'})} \langle \mathbf{S}_j \mathbf{S}_{j'} \rangle$ , i.e. excluding the on-site contribution. The overall agreement between Fig. 3(a) and Figs. 3(c), (e) is more than satisfactory, given that the variational phase diagram in fact involves two levels of approximation: (i) the effective model (10) was derived via perturbation theory to second order in electron hopping, (ii) the effective model was solved using a crude variational Ansatz. Moreover, the exact diagonalization for such a small cluster may be expected to overestimate the effect of quantum fluctuations, shifting the phase boundaries significantly. A comparison of the results for 4-, 6-, and 8-site cluster indeed shows a systematic trend of the PM/FQ boundary moving slightly up with increasing system size. Therefore, the Hubbard model calculation well confirms the topology of the phase diagram and a rough location of the phase boundaries observed in Fig. 3(a), suggesting additionally a smoother crossover between the high-spin AF phase and low-spin FQ phase.

Finally, Fig. 3(f) demonstrates, that the overall structure of the phase diagram does not change upon hole doping that we simulate by removing one or two electrons from our Hubbard system, corresponding formally to 12.5% and 25% doping. Though the data presented in Fig. 3(f) are necessarily plagued by large finite-size effects, we may anticipate roughly the same location of the PM/FQ phase boundary and a growth of the FQ phase at the expense of the AF phase. This trend is in line with intuition, since the FQ phase characterized by the dynamical mixing of  $s$  and  $\mathbf{T}$  can better accommodate the  $d^7$  mobile carriers and their interplay with the  $d^8$  background to be discussed in the next section. The FQ phase might be therefore energetically favorable to the AF one upon doping. On the other hand, from the same perspective there seems to be only a little difference between the FQ and PM phases.

### III. DOPED CASE: $d^7$ HOLES WITHIN $d^8$ BACKGROUND

In this section, the effective model will be completed by introducing mobile carriers represented by holes corresponding to the  $d^7$  configuration  $f$  shown in Fig. 1(c). We only include the  $d^7$  states with the single  $e_g$  electron occupying the  $3z^2 - r^2$  orbital. The participation of  $d^7$  configurations of  $x^2 - y^2$  character is partially suppressed by their higher energy due to  $\Delta$ , partially it is caused by on-site correlations preventing their motion even though the hopping amplitude associated with the  $x^2 - y^2$  orbital is three times larger than that of  $3z^2 - r^2$ . We will discuss these issues at relevant points later. As a result, the  $x^2 - y^2$  electrons “live” in the system mostly bound in the triplet  $d^8$  configurations.

In the following, we first discuss the derived interactions between the  $d^7$  and  $d^8$  objects in our model, then focus on the individual propagation of the doped holes, and finally examine their pairing tendencies and implications for possible superconductivity.

#### A. Interaction between holes and background

The interaction of the  $d^7$  holes with the  $d^8$  background consisting of  $s$  and  $T$  particles is derived in a straightforward way by projecting the electronic hopping on a  $d^7$ - $d^8$  bond onto the low-energy states constituting the basis of our model. It takes a form of  $f$  hopping accompanied by “counterflow” of  $d^8$  objects  $s$  and  $T$ , which may involve changes in their state or even an  $s \leftrightarrow T$  transition. Several sample processes of this kind are illustrated in Fig. 4.

To express the interaction in a compact form, we again utilize the bond  $d^8$  operators  $\tilde{S}_{ij}$  and  $S_{ij}$  defined by Eq. (9) and introduce new bond operators that capture the hopping of  $f$ . The first one is a regular spin-independent hopping

$$n_{ij} = f_{i\uparrow}^\dagger f_{j\uparrow} + f_{i\downarrow}^\dagger f_{j\downarrow}, \quad (15)$$

the second one involves the  $f$  spin and is defined via

$$\sigma_{ij}^\alpha = \sum_{s,s'=\uparrow,\downarrow} f_{is}^\dagger \sigma_{ss'}^\alpha f_{js'} \quad (16)$$

with  $\sigma^\alpha$  ( $\alpha = x, y, z$ ) denoting the Pauli matrices. In addition to transferring  $f$  between the sites, the latter operator performs either a flip of the  $f$  spin ( $\sigma^x$ ,  $\sigma^y$ ) or makes the hopping sensitive to the spin value ( $\sigma^z$ ). The final  $d^7$ - $d^8$  Hamiltonian reads as

$$\begin{aligned} \mathcal{H}_{d^7-d^8} = & \sum_{\langle ij \rangle} [\text{sgn}_{ij} A \sigma_{ij} \tilde{S}_{ji} + B \sigma_{ij} S_{ji} \\ & + n_{ij} (C_0 s_j^\dagger s_i + C_1 T_j^\dagger T_i)] + \text{H.c.} \quad (17) \end{aligned}$$

As in the case  $\mathcal{H}_{d^8}$  of Eq. (10), the form of the Hamiltonian  $\mathcal{H}_{d^7-d^8}$  is again explicitly spin-isotropic and in fact

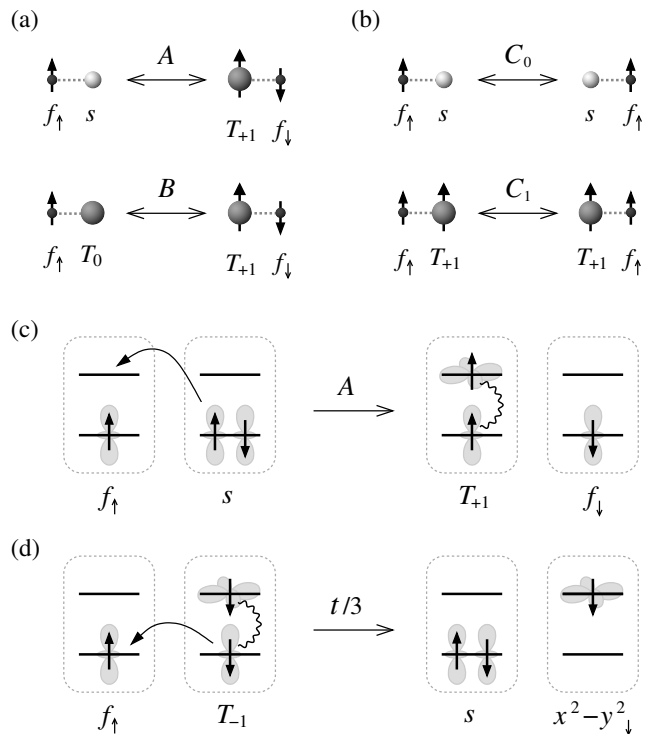


FIG. 4. Cartoon representation of the  $f$  particle motion through the  $d^8$  background, i.e. examples of  $d^7$ - $d^8$  bond processes contained in Eq. (17). (a) Hole hopping involving spin degrees of freedom: Within the process  $A$ , the hole hopping is entangled with a singlet-triplet transition; during process  $B$ , the hole exchanges its position with a triplon  $T$  in a spin-sensitive manner. (b) Spin-independent hole hopping: the hole exchanges its position with either a singlet  $s$  (process  $C_0$ ) or triplon  $T$  (process  $C_1$ ) without altering any spin state. (c) Process  $A$  depicted using the representation of the spin-orbital states as in Fig. 1(c). Its origin is the interorbital hopping of the electron from  $d^8$  to  $d^7$  site. The electron added to the  $x^2 - y^2$  orbital gets bound into a triplon  $T$  by virtue of Hund’s coupling. (d) Hopping process converting  $3z^2 - r^2$  hole  $f_\uparrow$  into a virtual  $(x^2 - y^2)_\downarrow$  fermion, at the energy cost of  $3J_H$  required to break  $S = 1$  triplet  $T$  state at the neighboring site.

dictated by this symmetry. Analogous forms of the interaction between holes and singlet-triplet background can be encountered e.g. in the context of hole-doped Heisenberg ladders or bilayers [21, 22] or in the context of spin-crossover cobaltates, where the triplons carry in addition an orbital degree of freedom [23, 24]. Following the microscopic derivation, the individual parameters entering (17) are given by

$$A = \frac{1}{\sqrt{6}} t \cos \theta, \quad B = \frac{1}{2} t, \quad C_0 = \frac{1}{3} t \cos^2 \theta, \quad C_1 = \frac{1}{2} t. \quad (18)$$

A few examples of different types of processes contained in  $\mathcal{H}_{d^7-d^8}$  are sketched in Fig. 4(a),(b). The most interesting one corresponds to the  $A$  term representing a hole hopping accompanied by  $s \leftrightarrow T$  transition. Ex-

panded in full, the relevant term  $\frac{1}{\sqrt{2}}\sigma_{ij}\tilde{\mathbf{S}}_{ji}$  takes the form

$$T_{-1j}^\dagger f_{i\uparrow}^\dagger f_{j\downarrow} + T_{0j}^\dagger \frac{1}{\sqrt{2}}(f_{i\uparrow}^\dagger f_{j\uparrow} - f_{i\downarrow}^\dagger f_{j\downarrow}) - T_{+1j}^\dagger f_{i\downarrow}^\dagger f_{j\uparrow} + \text{H.c.} \quad (19)$$

For brevity, we have omitted  $s_i$  in each contribution and used the  $\frac{1}{\sqrt{2}}$  prefactor. The  $A$  processes are essential to understand the effects arising due to the hole doping in the PM phase of the background. The dynamical generation and annihilation of triplet excitations  $\mathbf{T}$  by the doped hole has a profound impact on its propagation and leads to clear polaronic features discussed in Sec. III B. It may become also a source of hole pairing that is evaluated in Sec. III C. When focusing on the PM phase, the  $A$  processes need to be considered together with the processes linked to the parameter  $C_0$ , that just exchange the position of  $f$  and  $s$  on the bonds and provide therefore a free motion of  $f$  through the predominantly  $s$  background. The processes of corresponding to the  $B$  and  $C_1$  terms become important at larger  $T$  density and are thus relevant in case of the ordered  $d^8$  background that is beyond our scope here.

Another possibility of visualizing the hopping processes in  $\mathcal{H}_{d^7-d^8}$ —based on the schematic representation of the states of Fig. 1(c)—is used in Fig. 4(c). Starting with the  $f$  hole and its most frequent bond-neighbor  $s$  in the PM phase, the interorbital hopping can be easily associated with the  $A$  process.

We note that the hopping processes in the underlying  $e_g$  orbital Hubbard model allow a mixing of the  $f$  hole of  $3z^2-r^2$  symmetry with the  $d^7(x^2-y^2)$  states not included in our effective  $s$ - $T$ - $f$  model. Figure 4(d) shows such an example, where  $3z^2-r^2$  intraorbital hopping converts  $f$ -fermion into a virtual  $d^7(x^2-y^2)$  state. This process breaks  $S=1$  triplet bound state and costs a large energy of  $3J_H$ . As the latter far exceeds a mixing matrix element of  $t/3$ , admixture of  $x^2-y^2$  orbital into the  $f$ -fermion wave function is small and can be neglected. This is confirmed below by the ED analysis of the full  $e_g$  orbital Hubbard model. Thus in our effective  $s$ - $T$ - $f$  model, the  $x^2-y^2$  electrons are present only in a hidden form, i.e. bound in the triplon  $\mathbf{T}$  states of  $d^8$  configuration.

## B. Hole motion – renormalization within SCBA

In the previous section we found that the motion of doped holes proceeds via rather complex bond processes, where the hopping of  $d^7$  holes is intertwined in various ways with triplet excitations in the  $d^8$  background. The aim of this section is to analyze, how the coupling to the triplet excitations affects the motion of doped holes. We will focus specifically on the PM phase, where it is sufficient to consider just  $E_T$  and  $\kappa$  terms from  $\mathcal{H}_{d^8}$  (10) describing the magnetic background and  $A$  and  $C_0$  processes from the  $\mathcal{H}_{d^7-d^8}$  interaction Hamiltonian (17). The other terms that are higher-order in  $\mathbf{T}$  operators can be omitted in the PM phase due to the low triplon density.

The bare propagation of the doped holes ( $f$  particles) in the  $d^8$  background, which is mostly composed of  $s$  singlets in the PM phase, is captured by the  $C_0$  processes of (17) leading to the bare dispersion  $\varepsilon_{\mathbf{k}} = 2C_0(\cos k_x + \cos k_y)$ . The hopping amplitude  $C_0 \approx \frac{1}{3}t$  [see Eq. (18)] is derived from the weak  $3z^2-r^2$  intraorbital hopping, resulting in a small bare bandwidth. The holes couple to the triplet excitations represented as before by the triplons  $T_\alpha$  ( $\alpha = x, y, z$ ) of hardcore bosonic character, carrying the elementary excitations of the  $d^8$  background. The coupling is provided by the  $A$  term of (17), which transforms into the momentum representation as

$$\mathcal{H}_{d^7-d^8} \rightarrow iA \sum_{\mathbf{k}\mathbf{q}\alpha s s'} \eta_{\mathbf{k}-\mathbf{q}} T_{\alpha\mathbf{q}}^\dagger f_{\mathbf{k}-\mathbf{q},s}^\dagger \sigma_{s s'}^\alpha f_{\mathbf{k},s'} + \text{H.c.} \quad (20)$$

with  $\eta_{\mathbf{q}} = 2(\cos k_x - \cos k_y)$ . The approximate diagonalization of  $\mathcal{H}_{d^8}$  as described in Sec. II B leads to three degenerate eigenmodes  $\alpha_{\mathbf{q}}$  with the dispersion (14). The corresponding operators are constructed from  $T_{x,y,z}$  by Bogoliubov transformation  $T_{\alpha\mathbf{q}} = u_{\mathbf{q}}\alpha_{\mathbf{q}} + v_{\mathbf{q}}\alpha_{-\mathbf{q}}^\dagger$ , where the Bogoliubov factors take the form

$$u_{\mathbf{q}} = \frac{1}{\sqrt{2}} \sqrt{\frac{E_T + 4\kappa\gamma_{\mathbf{q}}}{\omega_{\mathbf{q}}} + 1}, \quad v_{\mathbf{q}} = \frac{2\kappa\gamma_{\mathbf{q}}}{\omega_{\mathbf{q}}u_{\mathbf{q}}}. \quad (21)$$

Inserted into Eq. (20), this gives the linear coupling of  $f$  to the excitations  $\alpha_{\mathbf{q}}$ :

$$\mathcal{H}_{d^7-d^8} \rightarrow iA \sum_{\mathbf{k}\mathbf{q}\alpha s s'} \Gamma_{\mathbf{k}\mathbf{q}} \alpha_{\mathbf{q}}^\dagger f_{\mathbf{k}-\mathbf{q},s}^\dagger \sigma_{s s'}^\alpha f_{\mathbf{k},s'} + \text{H.c.}, \quad (22)$$

with the formfactor  $\Gamma_{\mathbf{k}\mathbf{q}} = \eta_{\mathbf{k}-\mathbf{q}}u_{\mathbf{q}} - \eta_{\mathbf{k}}v_{\mathbf{q}}$ . The propagation of  $f$  through the  $d^8$  background including the coupling (22) to its excitations is treated within standard selfconsistent Born approximation (SCBA) scheme commonly used to address magnetic polarons (see e.g. [25–28]). For the case of a single hole, we get the self-energy

$$\Sigma(\mathbf{k}, E) = 3A^2 \sum_{\mathbf{q}} \Gamma_{\mathbf{k}\mathbf{q}}^2 \mathcal{G}(\mathbf{k}-\mathbf{q}, E - \omega_{\mathbf{q}}), \quad (23)$$

which enters the single-hole propagator  $\mathcal{G}(\mathbf{k}, E) = [E + i0^+ - \varepsilon_{\mathbf{k}} - \Sigma(\mathbf{k}, E)]^{-1}$  to be determined selfconsistently.

Presented in Fig. 5(a) is the corresponding spectral function  $A(\mathbf{k}, E) = -\pi^{-1} \text{Im} \mathcal{G}(\mathbf{k}, E)$  obtained for a representative parameter point that falls into the PM phase. The spectral function bears typical polaronic features. The bottom of the hole band around  $\mathbf{k} = M$  is only mildly affected, but the higher parts are strongly renormalized with the quasiparticle weight reduced by factor  $\approx 2-3$ . Compared to the bare dispersion, the total bandwidth is about two times smaller. The energy position of the onset of the damping and dispersion flattening correlates with  $E_T$ , in this case evaluated to  $\approx 0.29$  eV.

The spectral function resulting from the effective model is well confirmed by exact diagonalization of the

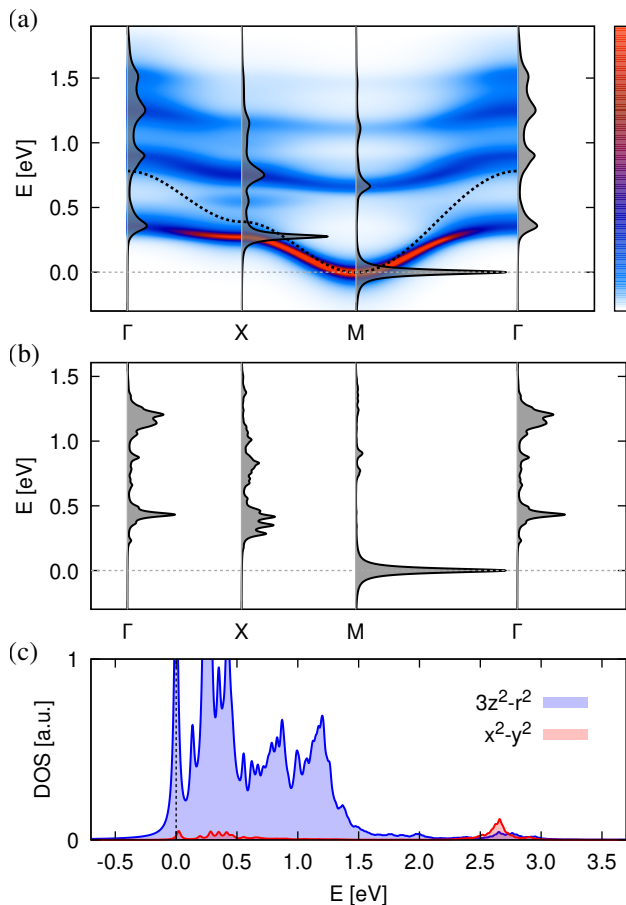


FIG. 5. (a) Single-hole spectral function obtained within SCBA applied to the effective  $s$ - $T$ - $f$  model. The parameter point corresponds to  $\Delta = 2$  eV and  $t = 0.3$  eV in Fig. 3(a). The spectral function is presented both in a form of a color map as well as profiles at selected high-symmetry points in the Brillouin zone. The dotted line shows the bare dispersion  $\varepsilon_{\mathbf{k}}$ . (b) Spectral function of a  $3z^2 - r^2$  hole obtained by exact diagonalization of the  $e_g$  Hubbard model at the 8-site cluster for the same parameter point. Both spectral functions were artificially broadened for an easier comparison and shifted to measure the energy from the bottom of the band. (c) Single-particle density of states (DOS) for the 8-site cluster resolved according to the contributing  $e_g$  orbital. The DOS corresponds to an average of the spectral function over the eight accessible momenta in the Brillouin zone.

underlying Hubbard model. In Fig. 5(b) we present the spectral function corresponding to an extraction of  $3z^2 - r^2$  electron

$$A_{\text{ED}}(\mathbf{k}, E) = -\frac{1}{\pi} \text{Im} \langle \text{GS} | z_{\mathbf{k}\sigma}^\dagger \frac{1}{E + i0^+ - \mathcal{H}_{\text{Hubb}}} z_{\mathbf{k}\sigma} | \text{GS} \rangle, \quad (24)$$

which may be directly compared to the  $f$  spectral function. The calculation was performed for the 8-site cluster of Fig. 3(d) used before.  $|\text{GS}\rangle$  denotes the cluster ground state. Given the smallness of the cluster and the approximations made in the derivation and treatment of the effective model, the agreement is very good. This

supports the picture that we have drawn based on the effective model, i.e. hole propagation along with intense generation and annihilation of the triplet excitations.

In Fig. 5(c) we return to the question of the relevance of the  $x^2 - y^2$  holes for the effective model, as discussed in the end of Sec. III A. Using the exact diagonalization of the Hubbard model, we can directly quantify the degree of their involvement. To this end, we study the orbital-resolved single-particle density of states, evaluated as an average of the corresponding spectral function over the cluster-compatible momenta  $\mathbf{k}$ :  $\text{DOS}(E) = N_{\mathbf{k}}^{-1} \sum_{\mathbf{k}} A(\mathbf{k}, E)$ . Here  $A(\mathbf{k}, E)$  is either the spectral function for the  $3z^2 - r^2$  hole presented for selected  $\mathbf{k}$  points in Fig. 5(b), or analogous one for the  $x^2 - y^2$  hole calculated as  $-\pi^{-1} \text{Im} \langle \text{GS} | x_{\mathbf{k}\sigma}^\dagger (E + i0^+ - \mathcal{H}_{\text{Hubb}})^{-1} x_{\mathbf{k}\sigma} | \text{GS} \rangle$ . As seen in Fig. 5(c), the DOS related to the  $x^2 - y^2$  hole is indeed negligible compared to the  $3z^2 - r^2$  one and is concentrated in two energy regions. The first one below approximately 0.5 eV covers essentially the range of the low-energy band of propagating  $3z^2 - r^2$  hole. This feature indicates a slight mixing of the  $x^2 - y^2$  and  $3z^2 - r^2$  holes stemming from the hole-type conversion processes discussed in the context of Fig. 4(d). The second region is located at energies higher by about  $\Delta$ , which corresponds to the expected excitation energy of the  $x^2 - y^2$  hole as compared to the  $3z^2 - r^2$  one.

### C. Hole pairing and BCS estimates

Focusing on the PM phase again, we now consider the dynamic generation and annihilation of triplet excitations as a source of pairing among the holes. We will follow the usual procedures applied in the theory of conventional superconductivity based on electron-phonon coupling and derive the hole-hole interaction by perturbatively eliminating the coupling Hamiltonian (17) that connects the  $d^7$  and  $d^8$  sectors, obtaining thereby the effective interaction acting in the  $d^7$  sector.

Specifically, from  $\mathcal{H}_{d^7-d^8}$  of Eq. (17) we again take the  $A$ -channel part, here in the form  $\sum_{ij} \text{sgn}_{ij} A \sigma_{ij} \tilde{S}_{ji}$ . The sum now runs through all nearest-neighbor  $i, j$  and includes thus also the H.c. counterpart of the bond sum in (17). The  $d^7$  hole operators are embedded in the bond operators  $\sigma_{ij}$  with the components given by (16), while the  $d^8$  sector is represented by  $\tilde{S}_{ji}$  defined by (9). By eliminating the above  $d^7$ - $d^8$  coupling via second-order perturbation theory, we obtain the effective interaction among  $f$ , which can be expressed in the form

$$\mathcal{H}_{f-f} \approx -A^2 \sum_{ij\alpha} \sum_{kl\beta} \text{sgn}_{ij} \text{sgn}_{kl} F_{ji,lk}^{\alpha\beta} \sigma_{ij}^\alpha \sigma_{kl}^\beta \quad (25)$$

with  $F$  being the  $\langle \tilde{S}\tilde{S} \rangle$  propagator evaluated entirely within the  $d^8$  sector. It is defined as the  $d^8$  ground-state average

$$F_{ji,lk}^{\alpha\beta} = \langle \text{GS} | \tilde{S}_{ji}^\alpha \frac{1}{\mathcal{H}_{d^8} - E_{\text{GS}}} \tilde{S}_{lk}^\beta | \text{GS} \rangle. \quad (26)$$

Recalling the similarity to the electron-phonon problem, the propagator  $F$  entering the hole-hole interaction is analogous to the static limit of the phonon propagator mediating effective electron-electron interaction. Thanks to the spin-space symmetry of the  $d^8$  background, the quantity (26) is isotropic,  $F_{ji, lk}^{\alpha\beta} = F_{ji, lk} \delta_{\alpha\beta}$ , and we need to consider just the diagonal elements  $F_{ji, lk}$  in the following. Note that by construction, the pairs of indices  $i, j$  and  $k, l$  correspond to nearest neighbors (NN) and we thus deal with a bond-bond correlator.

The evaluation of  $F_{ji, lk}$  for the PM phase is performed using an approximate solution of the  $d^8$  model limited to  $E_T$  and  $\kappa$  terms as in Sec. III B. One can proceed, for example, by converting (26) to the momentum representation and utilizing the previous description of the PM phase based on the Bogoliubov transformation of  $\mathcal{T}$ . For simplicity and to enable a transparent interpretation of the result, we will limit ourselves to an expansion to first order in  $\kappa/E_T$ , where  $F_{ji, lk}$  can be also easily evaluated using real-space perturbation theory and the contributions visualized in a pictorial way as done in Fig. 6(a)-(c). In this expansion, we start with the  $E_T$  part of  $\mathcal{H}_{d^8}$  of (10) as the unperturbed Hamiltonian and add the  $\kappa$ -interaction playing the role of the perturbation. Up to first order in  $\kappa/E_T$ , we get

$$F_{ji, lk} = \frac{1}{E_T} \left[ \delta_{il} - \frac{\kappa}{E_T} (\delta_{il}^{\text{NN}} + \frac{1}{2} \delta_{ik}^{\text{NN}} + \frac{1}{2} \delta_{jl}^{\text{NN}}) \right]. \quad (27)$$

The leading term of zeroth order contains standard Kronecker  $\delta_{il}$  which is equal to unity if  $i = l$ . The physical process behind this contribution to the effective  $f$ - $f$  interaction (25) is a creation of triplon by hopping of  $f$  during the first  $A$  process and its immediate absorption in the second  $A$  process [see Fig. 6(a) for a cartoon representation]. The possibility of such a pair hopping and the related kinetic energy gain drives the pairing of the holes into short-range pairs. Higher-order processes, that involve some action of  $\kappa$ , give rise to a more extended attraction of holes. In the first order included in (27), there are two physically distinct contributions that can be associated with the processes depicted in Fig. 6(b),(c). The first contribution corresponds to the term  $\delta_{il}^{\text{NN}}$  that checks whether the sites  $i$  and  $l$  form a nearest-neighbor bond. The process behind is similar to that of Fig. 6(a), but there is an extra hopping of the triplon between sites  $i$  and  $l$  in the intermediate state, which is provided by the  $\kappa$  interaction in the  $d^8$  sector. The second contribution, linked to the combination  $\frac{1}{2}(\delta_{ik}^{\text{NN}} + \delta_{jl}^{\text{NN}})$  in (27), has a completely different physical origin. It exploits the fact, that the  $\kappa$  interaction preforms singlet pairs of triplons  $\mathcal{T}$ , which may—through two correlated hoppings within the  $A$ -channel of  $\mathcal{H}_{d^7-d^8}$ —resonate with singlet pairs of holes. The triplon pairs appear with amplitude  $\propto \kappa/E_T$ , hence such processes appear as first-order in (27).

The next step is to insert the approximate  $F_{ji, lk}$  into (25) and collect all the possible process pathways. Here the real-space formulation proves quite helpful, as it enables to handle the various constraints explicitly. The

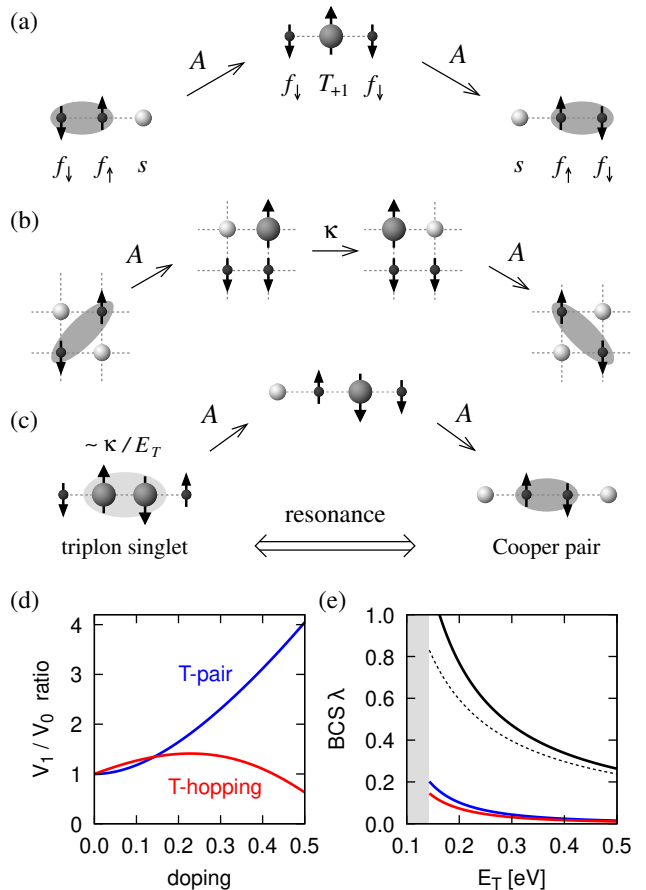


FIG. 6. (a) Cartoon representation of the dominant pairing process taking place on two adjacent bonds. One of the  $f$  holes undergoes  $A$  hopping leaving a triplon  $\mathcal{T}$  excitation behind, which is later absorbed by the other hole in the second  $A$  hopping. The amplitude of this process is proportional to  $A^2/E_T$ . (b),(c) Examples of additional pairing processes arising as corrections to (a) in the first order in  $\kappa/E_T$ . Process (b) is similar to (a) but with an extra hopping  $\kappa$  of the intermediate triplon  $\mathcal{T}$ . The process (c) corresponds to an absorption of a singlet pair of triplons  $\mathcal{T}$  (created via the  $\kappa$  exchange channel and having an amplitude  $\propto \kappa/E_T$ ) by a pair of  $f$  fermions. The absorption occurs via two  $A$  hoppings with the intermediate state containing one unpaired  $\mathcal{T}$ , hence its amplitude is  $\propto A^2/E_T$ . Such a hopping chain may proceed in both directions, leading to a promotion of  $f$  singlets by their resonance with the singlet triplon pairs fluctuating in the  $d^8$  background by virtue of the  $\kappa$  exchange. (d) Relative contribution of first-order terms to  $s$ -wave pairing potential (31) averaged over a circular Fermi surface at various doping levels. Following Eq. (31), the numbers have to be multiplied by  $\kappa/E_T$  when comparing the absolute pairing strength. (e) BCS  $\lambda$  for fixed  $t = 0.3$  eV and varying  $\Delta$  presented as function of  $E_T$  at doping level 0.25. Total value is shown as black solid line, contributions from  $V_0$ ,  $\mathcal{T}$ -hopping, and  $\mathcal{T}$ -pair first-order terms are shown as dashed/red/blue lines, respectively.  $E_T$  interval corresponding to long-range order is indicated by shading.

result is converted into momentum space and adapted to

the BCS form

$$\mathcal{H}_{\text{BCS}} \approx \sum_{\mathbf{k}\mathbf{k}'} V_{\mathbf{k}\mathbf{k}'} f_{\mathbf{k}\uparrow}^\dagger f_{-\mathbf{k}\downarrow}^\dagger f_{-\mathbf{k}'\downarrow} f_{\mathbf{k}'\uparrow}. \quad (28)$$

We have only picked up hole pairs with zero total momentum and the singlet pairing channel (triplet hole pairs come with an overall reduction by a factor of 3). The matrix elements  $V_{\mathbf{k}\mathbf{k}'}$  have somewhat complicated form, as the interaction reaches beyond NN due to the terms  $\propto \kappa/E_T$ . For convenience, we introduce two sets of symmetry-adapted functions used to capture the momentum dependence of pairing interaction in  $s$ -wave and  $d$ -wave channel. The  $s$ -wave symmetry functions read as

$$\begin{aligned} s_1 &= \cos k_x + \cos k_y, \\ s_2 &= \cos 2k_x + \cos 2k_y, \\ s_3 &= \cos 3k_x + \cos 3k_y, \\ s_4 &= \cos k_x \cos 2k_y + \cos 2k_x \cos k_y, \\ s_5 &= \cos k_x \cos k_y, \end{aligned} \quad (29)$$

while for the  $d$ -wave symmetry we define the following ones

$$\begin{aligned} d_1 &= \cos k_x - \cos k_y, \\ d_2 &= \cos 2k_x - \cos 2k_y, \\ d_3 &= \cos 3k_x - \cos 3k_y, \\ d_4 &= \cos k_x \cos 2k_y - \cos 2k_x \cos k_y. \end{aligned} \quad (30)$$

The matrix elements entering the pairing interaction are expressed following the structure of (27):

$$V_{\mathbf{k}\mathbf{k}'} = \frac{3A^2}{E_T} \left[ V_{0\mathbf{k}\mathbf{k}'} + \frac{\kappa}{E_T} V_{1\mathbf{k}\mathbf{k}'} + \mathcal{O}\left(\frac{\kappa^2}{E_T^2}\right) \right]. \quad (31)$$

In units of  $3A^2/E_T$ , the  $s$ -channel contribution of the zeroth and first order in  $\kappa/E_T$ , stemming from  $F_{ji,lk}$  of Eq. (27), reads as

$$\begin{aligned} V_{\mathbf{k}\mathbf{k}'}^{(s)} \approx & -2s_1s'_1 + \frac{\kappa}{E_T} \left[ -32s_5s'_5 + 8(s_2s'_5 + s_5s'_2) - 2s_2s'_2 \right. \\ & \left. - 4s_1s'_1 + 2(s_1s'_4 + s_4s'_1) - (s_1s'_3 + s_3s'_1) \right]. \end{aligned} \quad (32)$$

Here, the shorthand notations  $s_n$  and  $s'_n$  imply the corresponding functions from the set (29) with the argument  $\mathbf{k}$  or  $\mathbf{k}'$ , respectively. The first-order term ( $\propto \kappa/E_T$ ) in the first line comes from  $\mathbf{T}$ -hopping in the virtual state, the second line is due to the resonance between  $f$ -pairs and  $\mathbf{T}$ -pairs. Similarly, the  $d$ -wave contribution can be written as

$$\begin{aligned} V_{\mathbf{k}\mathbf{k}'}^{(d)} \approx & +6d_1d'_1 + \frac{\kappa}{E_T} \left[ -2d_2d'_2 \right. \\ & \left. - 4d_1d'_1 - 6(d_1d'_4 + d_4d'_1) - (d_1d'_3 + d_3d'_1) \right]. \end{aligned} \quad (33)$$

After specifying the pairing interaction, we now apply it in a situation with moderate hole doping  $\lesssim 0.3$ ,

where the  $d^8$  background is still expected to retain its specific features. The dispersion of the hole band is roughly parabolic with a minimum at  $\mathbf{k} = M$  point. Under such conditions, the leading term in the  $d$ -wave channel is obviously disfavored, we thus focus solely on the  $s$ -wave channel. Assuming nearly constant superconducting gap, we average the pairing potentials over  $M$ -centered circular Fermi surface according to the formula  $\langle V \rangle_{\text{FS}} = 1/(2\pi k_F)^2 \oint_{\text{FS}} d\mathbf{k} \oint_{\text{FS}} d\mathbf{k}' V_{\mathbf{k}\mathbf{k}'}$ , which is evaluated at various doping levels  $x$  entering through the Fermi radius  $k_F = \sqrt{2\pi x}$ . In Fig. 6(d) we first compare the relative contributions of the individual types of processes shown in Fig. 6(a)-(c) to the average  $\langle V_{\mathbf{k}\mathbf{k}'}^{(s)} \rangle_{\text{FS}} = V_0 + (\kappa/E_T)V_1$ . Relative to the leading term  $V_0$  associated with the process in Fig. 6(a), the total first order contribution [Fig. 6(b),(c) taken together] comes with a factor of about 3–4 multiplied additionally by  $\kappa/E_T$ . Considering the limitation of the latter ratio by the critical value  $\kappa/E_T = 1/8$ , the first-order contribution does not exceed about 30% of the total pairing strength in this approximation. Although this leaves the zeroth order dominant,  $T_c$  may be enhanced significantly by the two kinds of first-order processes. Among them, the pair resonance [Fig. 6(c)] takes over at larger doping levels.

We are now ready to make a rough BCS estimate. Plotted in Fig. 6(e) is the averaged pairing potential multiplied by the bare density of states  $1/4\pi C_0$ , forming together the BCS parameter  $\lambda$ :

$$\lambda = -\langle V_{\mathbf{k}\mathbf{k}'}^{(s)} \rangle_{\text{FS}} \frac{1}{4\pi C_0}. \quad (34)$$

Here,  $C_0$  is determined by hopping  $t$ , see Eq. (18). The data in Fig. 6(e) correspond to a representative  $t = 0.3\text{eV}$  cut through the phase diagram of Fig. 3(a). By varying  $\Delta$  as in Fig. 3(a), we mainly tune the parameter  $E_T$ . Its values are used in Fig. 6(e) instead of  $\Delta$  to produce a more transparent horizontal axis. As seen in Fig. 6(e), in the regime not very close to the PM/FQ phase boundary, the first-order contributions represent about 20% of the total  $\lambda$ . One can thus expect the higher-order terms in the pairing potential (31) to have a relatively minor effect. To make a conservative estimate, we take  $\lambda \approx 0.5$  for  $E_T = 0.3\text{eV}$  and insert it into the BCS formula  $T_c \approx 1.13\Omega \exp(-1/\lambda)$ . The cutoff  $\Omega$  is limited by the  $E_T$  value  $\approx 0.3\text{eV}$  but also by the quite small bandwidth. By setting for example  $\Omega \approx 0.1\text{eV}$ , we would arrive at  $T_c$  of about  $15\text{meV} \approx 180\text{K}$ . Even though such estimate is of course naive, the values of  $\lambda$  are promising for a potential superconductivity in nickel-based compounds displaying the spin-state crossover phenomenon. This is due to a rather strong coupling to triplet excitations with relatively high energy, combined with the enhanced density of states for a narrow band derived from the  $3z^2 - r^2$  orbital.

#### IV. CONCLUSIONS

We presented a basic theory for hole-doped nickelates containing low-spin  $d^8$   $\text{Ni}^{2+}$  ions on a square lattice. Such an ionic ground state may be stabilized by various means, e.g., by square-planar coordination of Ni ions, substitution of apical oxygens by halide ions, or by an extreme elongation of the  $\text{NiO}_6$  octahedra in the out-of-plane direction. We specifically focused on the spin-crossover regime, where—by a proper balance of the crystal field splitting and Hund’s coupling—the low-spin  $S = 0$  ionic state is quasidegenerate with the high-spin  $S = 1$  state. In this regime, the material would be described by a rich magnetic model of singlet-triplet type, that we have derived perturbatively and supported by exact diagonalization of the underlying Hubbard model based on  $e_g$  orbitals. After establishing the relevant phase diagram and excitation spectrum, we considered a doped material containing a moderate proportion of  $d^7$   $\text{Ni}^{3+}$  ions. By electronic hopping, these  $d^7$  configurations act as mobile hole-like carriers that show a non-trivial interplay with the  $d^8$  background that we studied following again a microscopically derived model. The propagation of the doped holes is found to be tightly intertwined with a dynamic creation and annihilation of triplet excitations (triplons) in the  $d^8$  background, leading e.g. to strong polaronic features in their spectral function. Most importantly, the processes involving triplet excitations generate an effective interaction among the holes, which provides a strong Cooper pairing, suggesting  $s$ -wave superconductivity in the spin-crossover materials.

Part of this pairing potential is contributed by an interesting new mechanism based on a resonance between the singlet pairs of doped holes and the singlet pairs of charge-neutral triplons created in the  $d^8$  background by virtue of the exchange interactions. This mechanism is generic to doped singlet-triplet models and though it brings a relatively small contribution in the studied case, it may be strong in situations with high densities of triplons entangled in total-singlet pairs, such as that encountered in the highly frustrated Kitaev-like singlet-triplet model developed in the context of  $d^4$  honeycomb ruthenates [29, 30]. In general, the exploration of the unconventional superconductivity in the spin-state crossover materials, especially in low-spin  $\text{Ni}^{2+}$   $d^8$  compounds is an attractive direction for future theoretical and experimental studies.

#### ACKNOWLEDGMENTS

We would like to thank M. Hepting and P. Puphal for fruitful discussions concerning the material aspects. J. Ch. was supported by the Czech Science Foundation (GAČR) under Project No. GA22-28797S and by the project Quantum Materials for Applications in Sustainable Technologies, Grant No. CZ.02.01.01/00/22.008/0004572. G. Kh. acknowledges support from the European Research Council under Advanced Grant no. 101141844 (SpecTera). Computational resources were provided by the e-INFRA CZ project (ID:90254), supported by the Ministry of Education, Youth and Sports of the Czech Republic.

- 
- [1] D. Li, K. Lee, B. Y. Wang, M. Osada, S. Crossley, H. R. Lee, Y. Cui, Y. Hikita, and H. Y. Hwang, Superconductivity in an infinite-layer nickelate, *Nature* **572**, 624 (2019).
- [2] H. Sun, M. Huo, X. Hu, J. Li, Z. Liu, Y. Han, L. Tang, Z. Mao, P. Yang, B. Wang, J. Cheng, D.-X. Yao, G.-M. Zhang, and M. Wang, Signatures of superconductivity near 80 K in a nickelate under high pressure, *Nature* **621**, 493 (2023).
- [3] G. Wang, N. N. Wang, X. L. Shen, J. Hou, L. Ma, L. F. Shi, Z. A. Ren, Y. D. Gu, H. M. Ma, P. T. Yang, Z. Y. Liu, H. Z. Guo, J. P. Sun, G. M. Zhang, S. Calder, J.-Q. Yan, B. S. Wang, Y. Uwatoko, and J.-G. Cheng, Pressure-induced superconductivity in polycrystalline  $\text{La}_3\text{Ni}_2\text{O}_{7-\delta}$ , *Phys. Rev. X* **14**, 011040 (2024).
- [4] E. K. Ko, Y. Yu, Y. Liu, L. Bhatt, J. Li, V. Thampy, C.-T. Kuo, B. Y. Wang, Y. Lee, K. Lee, J.-S. Lee, B. H. Goodge, D. A. Muller, and H. Y. Hwang, Signatures of ambient pressure superconductivity in thin film  $\text{La}_3\text{Ni}_2\text{O}_7$ , *Nature* **638**, 935 (2025).
- [5] G. Zhou, W. Lv, H. Wang, Z. Nie, Y. Chen, Y. Li, H. Huang, W.-Q. Chen, Y.-J. Sun, Q.-K. Xue, and Z. Chen, Ambient-pressure superconductivity onset above 40 K in  $(\text{La},\text{Pr})_3\text{Ni}_2\text{O}_7$  films, *Nature* **640**, 641 (2025).
- [6] Y. Zhu, D. Peng, E. Zhang, B. Pan, X. Chen, L. Chen, H. Ren, F. Liu, Y. Hao, N. Li, Z. Xing, F. Lan, J. Han, J. Wang, D. Jia, H. Wo, Y. Gu, Y. Gu, L. Ji, W. Wang, H. Gou, Y. Shen, T. Ying, X. Chen, W. Yang, H. Cao, C. Zheng, Q. Zeng, J. Guo, and J. Zhao, Superconductivity in pressurized trilayer  $\text{La}_4\text{Ni}_3\text{O}_{10-\delta}$  single crystals, *Nature* **631**, 531 (2024).
- [7] M. Zhang, C. Pei, D. Peng, X. Du, W. Hu, Y. Cao, Q. Wang, J. Wu, Y. Li, H. Liu, C. Wen, J. Song, Y. Zhao, C. Li, W. Cao, S. Zhu, Q. Zhang, N. Yu, P. Cheng, L. Zhang, Z. Li, J. Zhao, Y. Chen, C. Jin, H. Guo, C. Wu, F. Yang, Q. Zeng, S. Yan, L. Yang, and Y. Qi, Superconductivity in trilayer nickelate  $\text{La}_4\text{Ni}_3\text{O}_{10}$  under pressure, *Phys. Rev. X* **15**, 021005 (2025).
- [8] E. Zhang, D. Peng, Y. Zhu, L. Chen, B. Cui, X. Wang, W. Wang, Q. Zeng, and J. Zhao, Bulk superconductivity in pressurized trilayer nickelate  $\text{Pr}_4\text{Ni}_3\text{O}_{10}$  single crystals, *Phys. Rev. X* **15**, 021008 (2025).
- [9] P. Gütllich and H. A. Goodwin, eds., *Spin Crossover in Transition Metal Compounds I* (Springer, Berlin, 2004).
- [10] V. Pardo and W. E. Pickett, Pressure-induced metal-insulator and spin-state transition in low-valence layered nickelates, *Phys. Rev. B* **85**, 045111 (2012).

- [11] R. D. Smyth, J. N. Blandy, Z. Yu, S. Liu, C. V. Topping, S. J. Cassidy, C. F. Smura, D. N. Woodruff, P. Manuel, C. L. Bull, N. P. Funnell, C. J. Ridley, J. E. McGrady, and S. J. Clarke, High- versus low-spin  $\text{Ni}^{2+}$  in elongated octahedral environments:  $\text{Sr}_2\text{NiO}_2\text{Cu}_2\text{Se}_2$ ,  $\text{Sr}_2\text{NiO}_2\text{Cu}_2\text{S}_2$ , and  $\text{Sr}_2\text{NiO}_2\text{Cu}_2(\text{Se}_{1-x}\text{S}_x)_2$ , *Chem. Mater.* **34**, 9503 (2022).
- [12] K. Otszchi, H. Ogino, J. Shimoyama, and K. Kishio, New candidates for superconductors; a series of layered oxysulfides  $(\text{Cu}_2\text{S}_2)(\text{Sr}_{n+1}\text{M}_n\text{O}_{3n-1})$ , *J. Low Temp. Phys.* **117**, 729 (1999).
- [13] S. J. Clarke, P. Adamson, S. J. C. Herkelrath, O. J. Rutt, D. R. Parker, M. J. Pitcher, and C. F. Smura, Structures, physical properties, and chemistry of layered oxychalcogenides and oxypnictides, *Inorg. Chem.* **47**, 8473 (2008).
- [14] Y. Matsumoto, T. Yamamoto, K. Nakano, H. Takatsu, T. Murakami, K. Hongo, R. Maezono, H. Ogino, D. Song, C. M. Brown, C. Tassel, and H. Kageyama, High-pressure synthesis of  $\text{A}_2\text{NiO}_2\text{Ag}_2\text{Se}_2$  ( $\text{A}=\text{Sr},\text{Ba}$ ) with a high-spin  $\text{Ni}^{2+}$  in square-planar coordination, *Angew. Chem. Int. Ed.* **58**, 756 (2019).
- [15] M. Matsuda, K. Katsumata, A. Zheludev, S. M. Shapiro, and G. Shirane, Neutron scattering study in  $\text{BaNiO}_2$ , *J. Phys. Chem. Solids* **60**, 1121 (1999).
- [16] J. A. Alonso, M. J. Martínez-Lope, J. L. García-Muñoz, and M. T. Fernández-Díaz, A structural and magnetic study of the defect perovskite  $\text{LaNiO}_{2.5}$  from high-resolution neutron diffraction data, *J. Phys.: Condens. Matter* **9**, 6417 (1997).
- [17] S. Sachdev and R. N. Bhatt, Bond-operator representation of quantum spins: Mean-field theory of frustrated quantum Heisenberg antiferromagnets, *Phys. Rev. B* **41**, 9323 (1990).
- [18] S. Gopalan, T. M. Rice, and M. Sigrist, Spin ladders with spin gaps: A description of a class of cuprates, *Phys. Rev. B* **49**, 8901 (1994).
- [19] A. V. Chubukov and D. K. Morr, Phase transition, longitudinal spin fluctuations, and scaling in a two-layer antiferromagnet, *Phys. Rev. B* **52**, 3521 (1995).
- [20] T. Sommer, M. Vojta, and K. W. Becker, Magnetic properties and spin waves of bilayer magnets in a uniform field, *Eur. Phys. J. B* **23**, 329 (2001).
- [21] R. Eder, Dynamics of spin ladders, *Phys. Rev. B* **57**, 12832 (1998).
- [22] M. Vojta and K. W. Becker, Doped bilayer antiferromagnets: Hole dynamics on both sides of a magnetic ordering transition, *Phys. Rev. B* **60**, 15201 (1999).
- [23] J. Chaloupka and G. Khaliullin, Spin polaron theory for the photoemission spectra of layered cobaltates, *Phys. Rev. Lett.* **99**, 256406 (2007).
- [24] G. Khaliullin and J. Chaloupka, Origin of strong correlations and superconductivity in  $\text{Na}_x\text{CoO}_2$ , *Phys. Rev. B* **77**, 104532 (2008).
- [25] S. Schmitt-Rink, C. M. Varma, and A. E. Ruckenstein, Spectral function of holes in a quantum antiferromagnet, *Phys. Rev. Lett.* **60**, 2793 (1988).
- [26] C. L. Kane, P. A. Lee, and N. Read, Motion of a single hole in a quantum antiferromagnet, *Phys. Rev. B* **39**, 6880 (1989).
- [27] G. Martínez and P. Horsch, Spin polarons in the  $t$ - $J$  model, *Phys. Rev. B* **44**, 317 (1991).
- [28] J. H. Nyhegn, K. K. Nielsen, and G. M. Bruun, Equilibrium and nonequilibrium dynamics of a hole in a bilayer antiferromagnet, *Phys. Rev. B* **106**, 155160 (2022).
- [29] P. S. Anisimov, F. Aust, G. Khaliullin, and M. Daghofer, Nontrivial triplon topology and triplon liquid in Kitaev-Heisenberg-type excitonic magnets, *Phys. Rev. Lett.* **122**, 177201 (2019).
- [30] J. Chaloupka and G. Khaliullin, Highly frustrated magnetism in relativistic  $d^4$  Mott insulators: Bosonic analog of the Kitaev honeycomb model, *Phys. Rev. B* **100**, 224413 (2019).